FUDMA Journal of Sciences (FJS)
ISSN online: 2616-1370
ISSN print: 2645 - 2944
Vol. 10 No. 18, September, 2026, pp 181 –195
DOI: https://doi.org/10.33003/fjs-2026-1018-5562

Acanthus montanus Phytochemicals as Potential Multi-Target Therapeutics for Uterine Fibroids: An Integrated GC-MS, Network Pharmacology, and Molecular Dynamics Study

***[1]Mutiu A. Alabi, [1]Dauda S. Adebara, [1]Habeebullah A. Jamiu, [1]Abdullateef K. Ayuba, [2]Abdulhameed O. Alli, [1]Ronke A. Oluokun and [1]Emmanuel O. Ajani**

[1]Biochemistry Department, Faculty of Pure and Applied Sciences, Kwara State University, Malete, Kwara State, Nigeria.
[2]Department of Science Laboratory Technology, Institute of Applied Sciences, Kwara State Polytechnic, Ilorin, Kwara State, Nigeria.

*Corresponding authors' email: mutiu.alabi@kwasu.edu.ng

ABSTRACT

Uterine fibroids are benign hormone-responsive tumours characterized by dysregulated cellular proliferation, extracellular-matrix accumulation, and altered growth-factor signaling. This study investigated the potential anti-fibroid activity of Acanthus montanus leaf phytochemicals using an integrated computational approach. Ethanolic leaf extract was subjected to GC–MS profiling, followed by ADME/drug-likeness screening, network pharmacology, molecular docking, 100-ns molecular dynamics (MD) simulation, PASS activity prediction, and toxicity assessment. GC–MS identified 20 putative phytoconstituents, with 2,3-bis[(4-hydroxy-3-methoxyphenyl)methyl]butane-1,4-diol, tetramethyl ether showing 95% spectral similarity. Fourteen compounds (70%) exhibited high predicted gastrointestinal absorption, while the prioritized tetramethyl ether derivative showed favourable drug-likeness and no PAINS alerts. Network pharmacology identified 25 overlapping targets associated with uterine fibroids, with enrichment of PI3K-Akt, MAPK, estrogen, hormone-related, and other proliferation-associated pathways. Molecular docking showed that leuprolide had SP/XP scores of -8.290/-8.145 kcal/mol, whereas the tetramethyl ether derivative showed -4.772/-4.511 kcal/mol, with MM-GBSA values of -40.63/-55.42 kcal/mol for leuprolide and favourable binding interactions for the phytochemical. The 100-ns MD simulation demonstrated persistent protein–ligand contacts and maintained secondary structural elements, although substantial RMSD fluctuations indicated considerable conformational flexibility. PASS prediction suggested apoptosis agonist (Pa/Pi = 0.436/0.057), antineoplastic (0.264/0.123), ovulation inhibitor (0.482/0.068), and gonadotropin antagonist (0.445/0.035) activities. Predicted LD_{50} was 2000 mg/kg (toxicity class 4). A. montanus phytochemicals, particularly the tetramethyl ether derivative, demonstrate promising computational evidence for multitarget modulation of uterine fibroid-associated pathways. Experimental validation is required to establish efficacy, mechanism, and safety.

Received: 03 Aug. 2026
Accepted: 15 Aug. 2026
Published: 24 Sep. 2026

Keywords: *Acanthus montanus*, Uterine fibroid, GC-MS, ADME, Network pharmacology, Molecular docking, MD simulation

INTRODUCTION

Acanthus montanus (Nees) T. Anderson is a medicinal shrub of the family Acanthaceae found in Central and West Africa and has a history of use in African ethnomedicine. Its leaves and other plant parts have been used traditionally for conditions involving inflammation, pain, urinary and reproductive disorders, and other ailments (Idu et al., 2022; Okoli et al., 2008). Phytochemical investigations have demonstrated that the plant is chemically diverse, with reported constituents including alkaloids, flavonoids, phenolic compounds, terpenoids, steroids, saponins, and other secondary metabolites. More specific phytochemical investigations have also identified phenylethanoid glycosides, including acanmontanoside, together with other glycosides and triterpenoid constituents. These findings are relevant because the chemical diversity of *A. montanus* provides multiple structural classes that could potentially interact with different molecular targets involved in fibroid biology. Previous studies have further reported antioxidant, anti-inflammatory, antimicrobial, analgesic, and immunomodulatory activities of *A. montanus* extracts, providing pharmacological evidence for its biological activity (Idu et al., 2022; Okoli et al., 2008).

Despite this phytochemical and pharmacological evidence, the potential application of *A. montanus* specifically in uterine fibroid management remains poorly characterized. In particular, there is limited information on whether its constituents can interact with molecular targets central to fibroid development, including estrogen-related signaling, EGFR-mediated proliferation, AKT1-associated survival pathways, CDK4-dependent cell-cycle progression, and PARP1-associated cellular responses. This represents an important gap because the traditional use of the plant and its demonstrated biological activities do not, by themselves, establish a molecular basis for anti-fibroid activity. Furthermore, the presence of multiple chemically diverse constituents makes it difficult to identify promising compounds and predict their individual target interactions using conventional experimental screening alone.

Computational pharmacology is therefore particularly suitable for the preliminary investigation of *A. montanus*. Molecular docking can evaluate the ability of structurally diverse phytochemicals to occupy target-binding sites and

estimate their relative binding affinities (Aljawobaei et al., 2025; Asiamah et al., 2023), while molecular dynamics (MD) simulation can assess whether promising protein-ligand complexes remain structurally stable over time (Farhadi et al., 2025; Grewal et al., 2025). Network pharmacology complements these approaches by examining the relationships between multiple phytochemicals, molecular targets, and disease-associated pathways. ADME and toxicity prediction can further prioritize compounds with appropriate drug-like and safety characteristics before experimental testing. Such an integrated strategy is especially valuable for a chemically complex medicinal plant because it permits systematic prioritization of candidate compounds rather than treating the extract as a single pharmacological entity.

Accordingly, the present study investigated the potential anti-fibroid activity of *A. montanus* leaf phytochemicals using an integrated GC-MS, SwissADME, network pharmacology, molecular docking, molecular dynamics, PASS, and toxicity-prediction framework. The study specifically sought to identify phytochemical constituents with favorable drug-like properties, determine their associations with uterine fibroid-related molecular targets and pathways, characterize their binding interactions with selected target proteins, and evaluate the dynamic stability and predicted biological and toxicity profiles of the leading candidates. By connecting the phytochemical composition of *A. montanus* with molecular targets implicated in hormone-dependent proliferation, apoptosis, and fibrotic remodeling, this approach provides a mechanistic basis for prioritizing candidate compounds for subsequent experimental validation (Idu et al., 2022; Okoli et al., 2008).

MATERIALS AND METHODS

Plant Material Collection and Authentication

The study was conducted between December 2025 and July 2026. Fresh leaves of *Acanthus montanus* were collected from a local farm in Ilorin, Nigeria, in December 2025. The plant was identified and authenticated by Mr. Bolu Ajayi, a taxonomist, from the Plant Biology Department, University of Ilorin, Kwara State, Nigeria, with a voucher number UILH/001/1828/2025 and deposited at the herbarium for reference. The leaves were washed with running water, dried at 25-28 °C for 7 days, pulverized into powder with a grinder, and the powder was stored in airtight containers until further analysis.

Ethanol Extraction

Exactly 100 g of the powdered leaves were extracted by maceration process using 500 ml of ethanol for 48 h. The extract was concentrated with a rotary evaporator at a temperature of 40 °C, to yield an ethanol extract. The extract was thereafter dried in a hot air oven at 45 °C, weighed, and stored at 4 °C. The yield percentage was calculated as:

$$Percentage\ Yield = \frac{Weight\ of\ Extract}{Weight\ of\ Plant\ Powder} \times 100$$

Using 28.2 g of dried extract obtained from 100 g of powdered leaves, the extraction yield was 26.2% (w/w). The extraction procedure was therefore based on ethanol as the extraction solvent, 48 h maceration, and subsequent concentration at 40 °C.

GC-MS Analysis and Phytochemical Identification

The phytochemical composition of the ethanol extract was determined by gas chromatography-mass spectrometry (GC-MS). The extract was prepared at a concentration of 10 mg/mL in methanol and analyzed using a GC-MS system consisting of an Agilent 7890B gas chromatograph coupled to a 5977A mass selective detector.

Chromatographic separation was performed using an HP-5MS capillary column (30 m × 0.25 mm internal diameter, 0.25 μm film thickness), with helium as the carrier gas at a flow rate of 1 mL/min. The oven temperature was initially maintained at 50 °C for 2 min and subsequently increased to 280 °C at a rate of 10 °C/min, followed by a 10-min hold. An aliquot of 1 μL was injected in splitless mode at an injector temperature of 250 °C. Mass spectra were acquired in electron-ionization mode at 70 eV over an m/z range of 50-550.

Compounds were identified by comparing their mass spectra with reference spectra in the NIST mass spectral library, supplemented by retention-index information where available. To improve identification reliability, compounds with library similarity scores of ≥80% were regarded as putatively identified, whereas compounds with scores of 70-79% were considered tentative identifications. Compounds with library similarity scores below 70% were considered insufficiently supported for confident identification and were excluded from the principal compound-specific downstream analyses. Where more than one library candidate was assigned to the same chromatographic peak or retention time, the candidates were treated as alternative spectral matches rather than independent compounds unless chromatographic resolution supported their distinction.

Duplicate compound assignments were consolidated before subsequent ADME and network-pharmacology analyses. Compounds for which essential structural information, such as molecular formula, could not be established were not subjected to compound-specific computational analyses.

Retrieval of Compound Structures

The chemical structures of the retained GC-MS-identified compounds were obtained from the PubChem database using the corresponding compound names. Canonical SMILES or isomeric SMILES representations were retrieved for compounds with available structural records and used as input for subsequent computational analyses. Compounds without sufficiently reliable structural assignments were excluded from downstream structure-based analyses.

SwissADME-Based Pharmacokinetic and Drug-Likeness Analysis

The pharmacokinetic and drug-likeness properties of the retained phytochemicals were evaluated using the SwissADME web server. The analyzed parameters included gastrointestinal (GI) absorption, and drug-likeness according to the Lipinski, Ghose, Veber, Egan, and Muegge rules. Medicinal-chemistry parameter, including PAINS alert, were also evaluated. The BOILED-Egg model was used to estimate gastrointestinal absorption.

For screening purposes, compounds showing high predicted GI absorption with relatively few or no violations of the established drug-likeness rules and no major PAINS liabilities were classified as “Pass.” Compounds showing low predicted GI absorption and/or multiple drug-likeness violations were classified as “Fail.” This classification was used strictly as a computational screening criterion and was not interpreted as evidence that a compound classified as “Fail” lacks biological activity.

Importantly, binding-energy values were not used as ADME criteria, because binding affinity is evaluated during the molecular-docking stage. Duplicate GC-MS assignments were consolidated before ADME analysis to avoid counting the same compound more than once.

Network Pharmacology and Target Identification

Targets associated with the retained *A. montanus* phytochemicals were predicted using the SwissTargetPrediction platform. The 20 compounds submitted for target prediction were those retained after the GC-MS identification-confidence assessment, duplicate consolidation, and ADME screening.

Uterine-fibroid-associated genes were independently retrieved from GeneCards, OMIM, and Open Targets using uterine fibroid/uterine leiomyoma-related searches. The resulting disease-associated gene sets were combined after removal of duplicate gene entries.

The predicted phytochemical targets were intersected with the uterine-fibroid-associated genes to identify overlapping targets potentially linking *A. montanus* constituents with uterine fibroid pathogenesis. The resulting overlapping target genes were used for subsequent protein-protein interaction (PPI) and pathway analyses.

Protein-Protein Interaction and Pathway Enrichment Analysis

The identified overlapping targets were submitted to the STRING database for construction of a protein-protein interaction network using a medium interaction-confidence threshold (>0.4). This threshold was used to retain interactions supported by moderate combined evidence while limiting inclusion of weakly supported associations.

The resulting network was further analyzed using Cytoscape version 3.10.2. Compound-target, target-pathway, and compound-target-disease networks were constructed where appropriate. Network topology was evaluated using degree, betweenness, and closeness centrality to identify highly connected or potentially influential hub proteins.

Functional and pathway enrichment analyses were performed using relevant biological pathway databases, including KEGG and Reactome, to identify biological processes and signaling pathways potentially associated with the overlapping targets. Enrichment significance was evaluated using the statistical outputs generated by the respective analysis platform.

Molecular Docking

Ligand Preparation

The retained phytochemicals were prepared for molecular docking using LigPrep in Schrödinger Maestro. Molecular structures obtained from PubChem in SMILES format were imported into Maestro. Protonation states were generated using Epik over a physiological pH range of 7.4 ± 2.0, while relevant tautomers and stereoisomers were generated where applicable, with specified chiral centers retained. The resulting structures were energy-minimized using the OPLS4 force field.

Receptor Preparation

The epidermal growth factor receptor (EGFR) structure with PDB ID: 4R5S was retrieved from the Protein Data Bank and prepared using the Protein Preparation Wizard in Schrödinger Maestro. Missing hydrogen atoms were added, bond orders were assigned, and structural deficiencies were corrected. Relevant loops were refined, disulfide bonds were assigned, and water molecules located beyond 5 Å from the binding site were removed. The hydrogen-bonding network was optimized using PROPKA at pH 7.0. Restrained minimization was subsequently performed using the OPLS4 force field until an RMSD convergence criterion of 0.3 Å was reached. EGFR was selected for detailed docking because it emerged among the overlapping uterine-fibroid-associated targets and was identified as a highly connected target in the PPI/network analysis. Thus, docking against EGFR provided a structure-based assessment of the interaction potential of prioritized A. montanus phytochemicals with a network-prioritized molecular target.

Receptor Grid Generation and Molecular Docking

The receptor grid was generated using the Glide Grid Generation panel. Van der Waals scaling was set to 0.8 with a partial-charge cutoff of 0.15, and the grid was centered on the defined active-site region. Molecular docking was performed using both Glide Standard Precision (SP) and Glide Extra Precision (XP) protocols. Post-docking optimization was enabled according to the standard Glide workflow. Docking performance was evaluated using GlideScore, expressed in kcal/mol, with more negative values indicating comparatively more favorable predicted binding. The compounds were ranked according to their SP and XP docking scores, with MM-GBSA binding free-energy estimates and ligand-residue interaction profiles used as complementary criteria. Because docking scores are computational estimates, they were interpreted comparatively rather than as experimentally measured binding affinities. Leuprolide was retained as the reference compound used in the original computational workflow. Because leuprolide is structurally distinct from the small phytochemicals evaluated, comparisons with it were interpreted as computational reference comparisons rather than direct evidence of equivalent pharmacological behavior.

Binding-Interaction Analysis

The docking poses of the reference compound and prioritized phytochemicals were examined using two-dimensional and three-dimensional ligand-interaction representations. Hydrogen bonds, hydrophobic interactions, π-interactions, and other non-covalent contacts with amino acid residues within the binding pocket were recorded.

Particular attention was given to residues repeatedly involved in interactions with the prioritized compounds and surrounding residues. The interaction patterns were compared across the reference and phytochemical ligands to determine whether the compounds occupied similar regions of the EGFR binding cavity.

Molecular Dynamics Simulation

Molecular dynamics (MD) simulation was performed to evaluate the dynamic stability and persistence of interactions between the prioritized ligand and the selected protein target. The protein-ligand complex was subjected to a 100-ns MD simulation using the Desmond module of Schrödinger Maestro. Prior to the production run, the prepared complex was solvated using the TIP3P water model in an orthorhombic simulation box and neutralized with appropriate counterions. The system was equilibrated before commencement of the production simulation under the NPT ensemble at 300 K and 1.01325 bar. A Nose-Hoover thermostat and Martyna-Tobias-Klein barostat were used to maintain the temperature and pressure, respectively.

The trajectory generated during the 100-ns simulation was analyzed to assess the structural and conformational stability of the protein-ligand complex. Root mean square deviation (RMSD) was used to monitor changes in the protein backbone and ligand position relative to their initial structures throughout the simulation. Root mean square fluctuation (RMSF) was evaluated to determine residue-level flexibility, while the radius of gyration (Rg) was used to assess changes in the compactness of the protein structure. Protein-ligand

interaction analysis was performed throughout the trajectory to determine the persistence of hydrogen bonds, hydrophobic interactions, ionic interactions, and water-mediated contacts. The stability of the complex was assessed from the overall trajectory profile, with particular emphasis on the achievement of an equilibrated RMSD trajectory and persistence of ligand interactions within the binding pocket. The percentage occupancy of important protein-ligand contacts was calculated from the trajectory where applicable. The MD results were interpreted together with the molecular-docking and MM-GBSA findings to determine whether the prioritized ligand maintained a stable interaction with the target protein during the simulation.

PASS Activity Prediction

The biological activity spectrum of the prioritized compounds was evaluated using the PASS (Prediction of Activity Spectra for Substances) online server. PASS estimates the probability of biological activities based on structural similarity to compounds with known activity profiles.

A Pa value >70% was used as the predefined threshold for highlighting predicted activities. Particular attention was given to predicted activities potentially relevant to uterine fibroid biology, including apoptosis-related, antineoplastic, endocrine-modulating, and reproductive-system-related activities.

PASS predictions were interpreted as computational hypotheses rather than experimental evidence of biological activity.

In Silico Toxicity Prediction

Potential toxicity liabilities of the prioritized compounds were evaluated using ProTox-3.0 and StopTox. ProTox-3.0 was used to predict oral acute toxicity, including predicted LD_{50} values and corresponding toxicity classes (I-VI), together with available toxicity endpoints generated by the platform. StopTox was used to identify predicted acute and chronic toxicity liabilities and structural alerts, including dermal toxicity, skin sensitization, skin irritation/corrosion, eye irritation/corrosion, and inhalation-related toxicity.

The toxicity predictions were used as preliminary safety-screening information. A predicted toxicity class or structural alert was not interpreted as proof of toxicity in humans or experimental animals, and computational predictions were considered insufficient to replace experimental toxicological evaluation.

Data Visualization and Statistical/Computational Interpretation

Docking interaction maps and molecular structures were visualized using BIOVIA Discovery Studio Visualiser v25. Network and pathway analyses were visualized using Cytoscape and the respective enrichment-analysis platforms. Computational results were interpreted comparatively across compounds and targets. In particular, docking scores, MM-GBSA estimates, molecular-interaction patterns, MD stability parameters, pharmacokinetic predictions, biological activity probabilities, and toxicity predictions were considered collectively when prioritizing compounds for further investigation.

RESULTS AND DISCUSSION

Ethanol Extraction Yield

Extraction of *Acanthus montanus* leaves with ethanol yielded 28.2% (w/w) of crude extract. This yield was slightly higher than the 25.58% (w/w) reported for ethanol extraction of *A. montanus* leaves by Oshadu et al. (2022), who obtained 255.84 g of extract from 1,000 g of starting plant material. The approximately 2.62-percentage-point increase observed in the present study may reflect differences in plant material, geographic origin, harvesting conditions, particle size, solvent-to-sample ratio, extraction duration, or other processing conditions. Nevertheless, the relatively comparable yields indicate that ethanol efficiently recovered extractable constituents from *A. montanus* leaves under the conditions employed in both studies.

GC-MS Chromatographic Profile

GC-MS analysis of the *Acanthus montanus* ethanolic extract revealed 20 putatively or tentatively identified compounds, with retention times ranging from 12.380 to 19.750 min and library similarity scores of 70-98% (Table 1). The identified constituents comprised predominantly terpenoids, fatty acids, long-chain alcohols, aldehydes, esters, and oxygenated aromatic compounds. The highest library match was observed for n-hexadecanoic acid (98%), followed by neophytadiene (96%), E,E,Z-1,3,12-nonadecatriene-5,14-diol (95%), and 2,3-bis[(4-hydroxy-3-methoxyphenyl)methyl]butane-1,4-diol, tetramethyl ether (95%). Other prominent high-confidence identifications included 12-methyl-E,E-2,13-octadecadien-1-ol (92%), 2-methyl-Z,Z-3,13-octadecadienol (92%), 3,7,11,15-tetramethyl-2-hexadecen-1-ol (91%), (-)-trans-pinane (90%), tridecanoic acid (90%), and supraene (89%). Compounds with intermediate library agreement included 5-nonadecen-1-ol (72%), the oxirane derivative (74%), 2-hydroxy-4-methoxybenzaldehyde pentyl ether (76%), and 7,11-hexadecadienal (70%) and were therefore regarded as tentative identifications. Several compounds occurred at the same retention time but represented alternative library assignments for the corresponding chromatographic peak, particularly at 12.380, 14.646, 14.886, 15.000, 15.773, and 19.738-19.750 min.

Table 1: Phytochemicals in *A. Montanus* Ethanolic Extract by GC-MS

S/N	Peak No.	RT (min)	Library identification	Library match (%)	Molecular formula	MW (g/mol)
1	5	12.38	Neophytadiene	96	$C_{20}H_{38}$	278.52
2	5	12.38	(-)-trans-Pinane	91	$C_{10}H_{18}$	138.25
3	5	12.38	Bicyclo[3.1.1]heptane, 2,6,6-trimethyl-, (1α,2β,5α)-	76	$C_{10}H_{18}$	138.25
4	7	12.597	5-Nonadecen-1-ol	72	$C_{19}H_{38}O$	282.51
5	10	13.518	n-Hexadecanoic acid	98	$C_{16}H_{32}O_2$	256.42
6	10	13.518	Tridecanoic acid	90	$C_{13}H_{26}O_2$	214.35
7	13	14.646	3,7,11,15-Tetramethyl-2-hexadecen-1-ol	91	$C_{20}H_{40}O$	296.54
8	13	14.646	(-)-trans-Pinane	90	$C_{10}H_{18}$	138.25
9	14	14.886	12-Methyl-E,E-2,13-octadecadien-1-ol	92	$C_{19}H_{36}O$	280.5
10	14	14.886	2-Methyl-Z,Z-3,13-octadecadienol	92	$C_{19}H_{36}O$	280.5
11	16	15	E,E,Z-1,3,12-Nonadecatriene-5,14-diol	95	$C_{19}H_{34}O_2$	294.5

S/N	Peak No.	RT (min)	Library identification	Library match (%)	Molecular formula	MW (g/mol)
12	16	15	Methyl 9-cis,11-trans-octadecadienoate	89	$C_{19}H_{34}O_2$	294.5
13	16	15	7,11-Hexadecadienal	70	$C_{16}H_{28}O$	236.39
14	19	15.727	Oxirane, 2,2-dimethyl-3-(3,7,12,16,20-pentamethyl-3,7,11,15,19-heneicosapentaenyl)-, (all-E)-	74	$C_{30}H_{50}O$	426.73
15	20	15.773	1,3,3-Trimethyl-2-hydroxymethyl-3,3-dimethyl-4-(3-methylbut-2-enyl)-cyclohexene	90	$C_{15}H_{26}O$	250.42
16	20	15.773	Supraene	89	$C_{30}H_{50}$	410.72
17	20	15.773	β-Bisabolenol	83	$C_{15}H_{26}O$	222.37
18	25	19.738	2,3-Bis[(4-hydroxy-3-methoxyphenyl)methyl]butane-1,4-diol, tetramethyl ether	95	$C_{20}H_{26}O_6$	362.4
19	25	19.738	2-Hydroxy-4-methoxybenzaldehyde, pentyl ether	76	$C_{13}H_{18}O_3$	222.28
20	26	19.75	2-Hydroxy-4-methoxybenzaldehyde, 2-methylpropyl ether	70	$C_{12}H_{16}O_3$	208.25

In Silico ADME and Drug-Likeness Profiling of *Acanthus Montanus* Phytochemicals

SwissADME analysis of the 20 GC-MS-identified phytochemicals revealed variable predicted gastrointestinal (GI) absorption and drug-likeness profiles (Table 2). Six compounds (30%) exhibited low predicted GI absorption and were classified as Fail, namely neophytadiene, (-)-trans-pinane, bicyclo[3.1.1]heptane, 2,6,6-trimethyl-, 5-nonadecen-1-ol, 3,7,11,15-tetramethyl-2-hexadecen-1-ol, and 3-eicosyne. These compounds showed between two and three drug-likeness violations involving the Lipinski, Ghose, Veber, Egan, and/or Muegge criteria. In contrast, 14 compounds (70%) showed high predicted GI absorption and were classified as Pass. These included *n*-hexadecanoic acid, tridecanoic acid, 12-methyl-E,E-2,13-octadecadien-1-ol, 2-methyl-Z,Z-3,13-octadecadienol, *E,E,Z*-1,3,12-nonadecatriene-5,14-diol, methyl 9-*cis*,11-*trans*-octadecadienoate, 7,11-hexadecadienal, the oxirane derivative, 1,3,3-trimethyl-2-hydroxymethyl-3,3-dimethyl-4-(3-methylbut-2-enyl)-cyclohexene, supraene, β-bisabolenol, the tetramethyl ether derivative, 2-hydroxy-4-methoxybenzaldehyde pentyl ether, and 2-hydroxy-4-methoxybenzaldehyde 2-methylpropyl ether. Among the Pass compounds, three showed no drug-likeness violations: 2,3-bis[(4-hydroxy-3-methoxyphenyl)methyl]butane-1,4-diol, tetramethyl ether; 2-hydroxy-4-methoxybenzaldehyde, pentyl ether; and 2-hydroxy-4-methoxybenzaldehyde, 2-methylpropyl ether. The remaining Pass compounds showed between one and two reported violations, predominantly involving the Muegge, Lipinski, Ghose, or Veber criteria. Importantly, none of the 20 evaluated phytochemicals showed PAINS alerts, indicating an absence of predicted pan-assay interference liabilities under the applied SwissADME screening.

Table 2: ADME Prediction of Phytochemicals with Pass/Fail Rules

S. No.	Compound Name	GI absorption	Druglikeness (#violations)	PAINS (#alerts)	Remark
1.	Neophytadiene	Low	2 (Lipinski, Ghose, Veber, Egan, Muegge - multiple violations)	0	Fail
2.	(-)-trans-Pinane	Low	2 (Lipinski, Ghose, Muegge)	0	Fail
3.	Bicyclo[3.1.1]heptane, 2,6,6-trimethyl-, (1α,2β,5α)-	Low	2 (Lipinski, Ghose, Muegge)	0	Fail
4.	5-Nonadecen-1-ol	Low	3 (Lipinski, Ghose, Veber, Egan, Muegge)	0	Fail
5.	n-Hexadecanoic acid	High	1 (Lipinski, Veber, Muegge)	0	Pass
6.	Tridecanoic acid	High	1 (Veber, Muegge)	0	Pass
7.	3,7,11,15-Tetramethyl-2-hexadecen-1-ol	Low	2 (Lipinski, Ghose, Veber, Muegge)	0	Fail
8.	3-Eicosyne	Low	2 (Lipinski, Ghose, Veber, Muegge)	0	Fail
9.	12-Methyl-E,E-2,13-octadecadien-1-ol	High	2 (Lipinski, Ghose, Veber, Muegge)	0	Pass
10.	2-Methyl-Z,Z-3,13-octadecadienol	High	2 (Lipinski, Ghose, Veber, Muegge)	0	Pass
11.	E,E,Z-1,3,12-Nonadecatriene-5,14-diol	High	1 (Veber, Muegge)	0	Pass
12.	Methyl 9-cis,11-trans-octadecadienoate	High	1 (Lipinski, Ghose, Veber, Muegge)	0	Pass
13.	7,11-Hexadecadienal	High	2 (Veber, Muegge)	0	Pass
14.	Oxirane, 2,2-dimethyl-3-(3,7,12,16,20-pentamethyl-3,7,11,15,19-heneicosapentaenyl)-, (all-E)-	High	1 (Lipinski, Ghose, Veber, Muegge)	0	Pass
15.	1,3,3-Trimethyl-2-hydroxymethyl-3,3-dimethyl-4-(3-methylbut-2-enyl)-cyclohexene	High	1 (Muegge)	0	Pass
16.	Supraene	High	1 (Muegge)	0	Pass
17.	β-Bisabolenol	High	2 (Muegge, plus others)	0	Pass
18.	2,3-Bis[(4-hydroxy-3-methoxyphenyl)methyl]butane-1,4-diol, tetramethyl ether	High	0	0	Pass
19.	2-Hydroxy-4-methoxybenzaldehyde, pentyl ether	High	0	0	Pass
20.	2-Hydroxy-4-methoxybenzaldehyde, 2-methylpropyl ether	High	0	0	Pass

Network Pharmacology

Evidence of Shared Molecular Targets Between Phytochemicals from Acanthus Montanus Extract and Uterine Fibroid-Related Genes

SwissTargetPrediction identified 970 potential protein targets associated with the phytochemicals retained from the *Acanthus montanus* extract, while 227 uterine fibroid-related genes were compiled from the disease-associated databases used in the study. Intersection analysis was performed using Venny 2.1, resulting in 25 overlapping target genes shared between the phytochemical-predicted targets and uterine fibroid-related genes (Figure 1). As shown in the Venn diagram, 945 targets (80.6%) were unique to the phytochemical target set, 202 genes (17.2%) were unique to the uterine fibroid disease-gene set, and 25 genes (2.1%) were common to both datasets. Thus, the 25 overlapping genes represented 2.6% of the 970 predicted phytochemical targets and 11.0% of the 227 uterine fibroid-associated genes, respectively. These shared targets were subsequently considered potential molecular mediators linking the phytochemicals of A. montanus with uterine fibroid pathogenesis and were used for downstream protein-protein interaction and pathway-enrichment analyses.

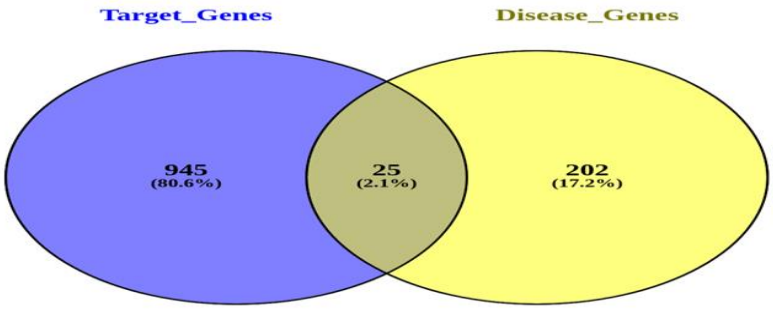

Figure 1: Venn diagram showing the intersection between A. montanus phytochemical-predicted targets and uterine fibroid-associated genes

Protein-Protein Interaction Network Analysis of Overlapping Targets Identified for Acanthus montanus in Uterine Fibroids

The STRING protein-protein interaction (PPI) network illustrates the interconnectedness of the predicted molecular targets of *Acanthus montanus* phytochemicals associated with uterine fibroids (Figure 2). The network shows a densely interconnected core comprising proteins involved in PI3K-related signaling, cell-cycle regulation, DNA repair, hormone signaling, and growth-related pathways, including PIK3CA, PIK3CB, PIK3CD, PIK3R1, PIK3R2, PIK3R3, CDK4, ESR2, PGR, EGFR-related signaling proteins, PARP1, TYMS, BLM, and DNMT3A. The PIK3CA/PIK3CB/PIK3CD and PIK3R1/PIK3R2/PIK3R3 cluster forms a particularly prominent interconnected region, suggesting substantial functional connectivity within the network. Other targets, including ESR2, PGR, CDK4, PARP1, TERT, RET, CASR, KIT, and GNHRR, are connected to multiple proteins within the network, indicating their potential involvement in several interacting biological processes relevant to uterine fibroid development. In contrast, METAP1 and THRB appear more peripheral, with fewer visible connections to the central network.

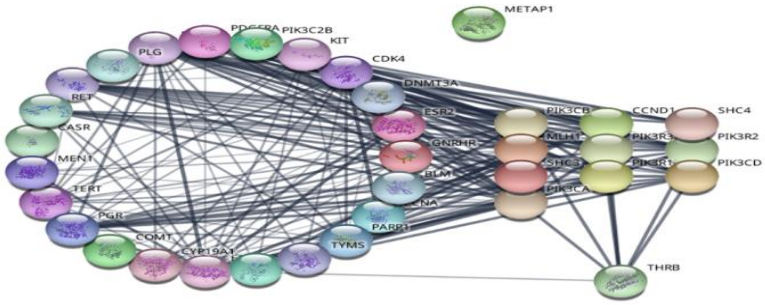

Figure 2: STRING PPI network of the the phytochemicals from *Acanthus montanus* in uterine fibroids

ShinyGO-Based Enrichment and Protein Interaction Analysis of Candidate Targets

Figure 3 presents the pathway enrichment analysis and interaction network of the 25 overlapping target genes identified for *Acanthus montanus*-associated uterine fibroid targets. The ShinyGO analysis revealed significant enrichment of pathways related to central carbon metabolism in cancer, non-small cell lung cancer, melanoma, endocrine resistance, breast cancer, glioma, EGFR tyrosine kinase inhibitor resistance, estrogen signaling, hepatocellular carcinoma, PI3K-Akt, MAPK, Ras, Rap1, calcium, hormone, and microRNA signaling pathways. Central carbon metabolism in cancer showed the highest fold enrichment (approximately 65-fold), followed by non-small cell lung cancer (approximately 65-fold) and melanoma (approximately 50-fold), whereas breast cancer, endocrine resistance and glioma showed fold enrichments of approximately 38-40-fold (Figure 3b). The statistical significance of the enriched pathways was high, with reported FDR values ranging from 8.9×10^{-9} for pathways in cancer to 2.9×10^{-3} for gastric cancer and phospholipase D signaling, while breast cancer and central carbon metabolism in cancer both showed an FDR of approximately 3.4×10^{-7}. Other notable pathways included PI3K-Akt signaling (3.4×10^{-5}),

MAPK signaling (1.8×10^{-4}), estrogen signaling (1.8×10^{-4}), hormone signaling (6.0×10^{-4}), EGFR tyrosine kinase inhibitor resistance (6.0×10^{-4}), Ras signaling (7.5×10^{-4}), calcium signaling (9.1×10^{-4}), and microRNAs in cancer (1.9×10^{-3}). The network representation further highlighted AKT1, EGFR, and ESR1 as important hub proteins linking several of the enriched pathways. Collectively, these findings indicate that the overlapping targets of A. montanus phytochemicals are associated with interconnected hormonal, estrogen-responsive, EGFR/PI3K-Akt, MAPK, Ras, and cancer-related signaling pathways, providing a mechanistic basis for subsequent molecular docking against EGFR.

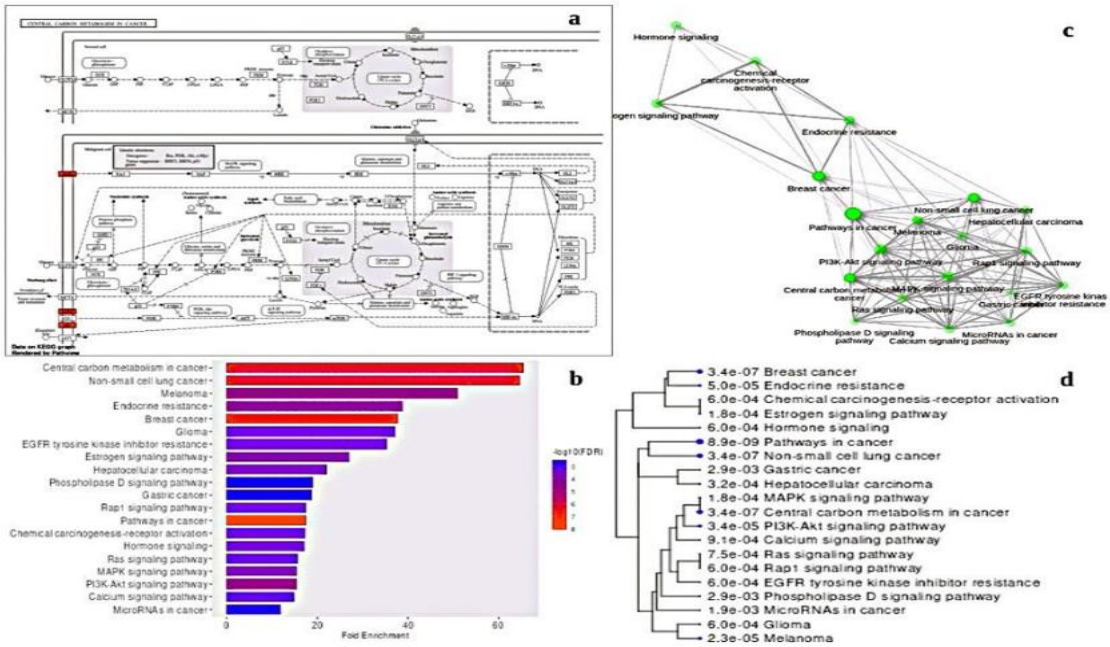

Figure 3: Enrichment analysis and PPI network of overlapping targets genes by ShinyGO. (a) Enriched KEGG pathway showing the hierarchical tree plot of significant genes. (b) Bar plot of significance pathway ($-\log_{10}$(FDR)). (c) Hub proteins AKT1, EGFR, and ESR1 shown by STRING network. (d) Integrated KEGG pathway map highlighting key targets in central carbon metabolism and oncogenic signaling.

Molecular Docking Analysis

Docking Scores and MM-GBSA Binding Free Energies of Top Hits

Using leuprolide as the reference drug, the 14 prioritized *A. montanus* phytochemicals showed variable binding affinities toward the selected target (Table 3). Leuprolide demonstrated the most favorable docking performance, with a Glide SP score of -8.290 kcal/mol, XP score of -8.145 kcal/mol, and corresponding MM-GBSA ΔG Bind values of -40.63 and -55.42 kcal/mol, respectively. Among the phytochemicals, 2,3-bis[(4-hydroxy-3-methoxyphenyl)methyl]butane-1,4-diol, tetramethyl ether showed the strongest and most consistent docking performance, with SP and XP scores of -4.772 and -4.511 kcal/mol, respectively. Supraene exhibited the most favorable MM-GBSA values among the phytochemicals (-44.64 kcal/mol SP; -47.39 kcal/mol XP), although its docking scores were weaker than those of the leading compound.

Table 3: Glide Standard Precision (SP) and Extra Precision (XP) Docking Scores (Gscore) with Corresponding MM-GBSA Binding Free Energies (kcal/mol) of the Top Ten Hit Compounds from *Acanthus Montanus* and the Reference Compound (Leuprolid).

S/No	Compound name	SP GScore (kcal/mol)	SP MM-GBSA ΔG Bind (kcal/mol)	XP GScore (kcal/mol)	XP MM-GBSA ΔG Bind (kcal/mol)
1	n-Hexadecanoic acid	1.099	-26.30	-1.006	-28.41
2	Tridecanoic acid	-1.252	-25.69	-2.083	-26.01
3	12-Methyl-E,E-2,13-octadecadien-1-ol	0.023	-38.08	-1.906	-41.63
4	2-Methyl-Z,Z-3,13-octadecadienol	-1.365	-34.64	0.160	-25.85
5	E,E,Z-1,3,12-Nonadecatriene-5,14-diol	-0.637	-39.38	-2.985	-37.48
6	Methyl 9-cis,11-trans-octadecadienoate	0.231	-38.70	-1.803	-32.88
7	7,11-Hexadecadienal	0.557	-34.44	-1.609	-33.89
8	Oxirane, 2,2-dimethyl-3-(3,7,12,16,20-pentamethyl-3,7,11,15,19-heneicosapentaenyl)-, (all-E)-	-3.956	-41.32	0.784	-37.80

S/No	Compound name	SP GScore (kcal/mol)	SP MM-GBSA ΔG Bind (kcal/mol)	XP GScore (kcal/mol)	XP MM-GBSA ΔG Bind (kcal/mol)
9	1,3,3-Trimethyl-2-hydroxymethyl-3,3-dimethyl-4-(3-methylbut-2-enyl)-cyclohexene	-3.821	-29.81	-2.806	-29.73
10	Supraene	-3.758	-44.64	-2.010	-47.39
11	β-Bisabolenol	-3.661	-34.83	-3.042	-21.47
12	2,3-Bis[(4-hydroxy-3-methoxyphenyl)methyl]butane-1,4-diol, tetramethyl ether	-4.772	-38.65	-4.511	-31.42
13	2-Hydroxy-4-methoxybenzaldehyde, pentyl ether	-3.709	-29.01	-3.787	-17.19
14	2-Hydroxy-4-methoxybenzaldehyde, 2-methylpropyl ether	-4.578	-32.02	-3.525	-28.09
15	Leuprolide (Reference)	-8.290	-40.63	-8.145	-55.42

Binding Mode Analysis of the Standard and Hit Phytocompounds against the Fibroid-Related Target Protein

The binding-mode analysis revealed distinct but complementary interactions between the reference ligand, leuprolide, and the prioritized *Acanthus montanus* phytochemical, 2,3-bis[(4-hydroxy-3-methoxyphenyl)methyl]butane-1,4-diol, tetramethyl ether, within the target-protein binding pocket. Leuprolide established a network of hydrogen-bonding and hydrophobic contacts with residues surrounding the binding site, indicating extensive accommodation of the peptide ligand within the receptor pocket (Figure 4). The 2D interaction map further demonstrated conventional hydrogen bonding together with carbon-hydrogen and π-alkyl interactions, while the 3D hydrophobic-surface representation showed that the ligand was favourably positioned within a mixed hydrophobic-hydrophilic pocket.

In comparison, the prioritized phytochemical exhibited a broader pattern of residue contacts (Figure 5), involving conventional hydrogen bonds, carbon-hydrogen interactions, π-alkyl contacts, salt-bridge/attractive-charge interactions, and hydrophobic contacts. The interaction map indicates contacts involving LYS860, ASP761, GLU865, GLU866, TYR764, LEU861, LEU833, ALA864, ARG831/832 and ASP830, among other surrounding residues. The multiple hydrogen-bond interactions, particularly those involving the acidic and polar residues of the binding region, suggest that the phytochemical was capable of establishing stabilizing polar interactions in addition to hydrophobic contacts. The 3D representation further shows that the ligand is deeply accommodated within the binding cavity and surrounded by regions of varying hydrophobicity, supporting favourable occupation of the binding pocket.

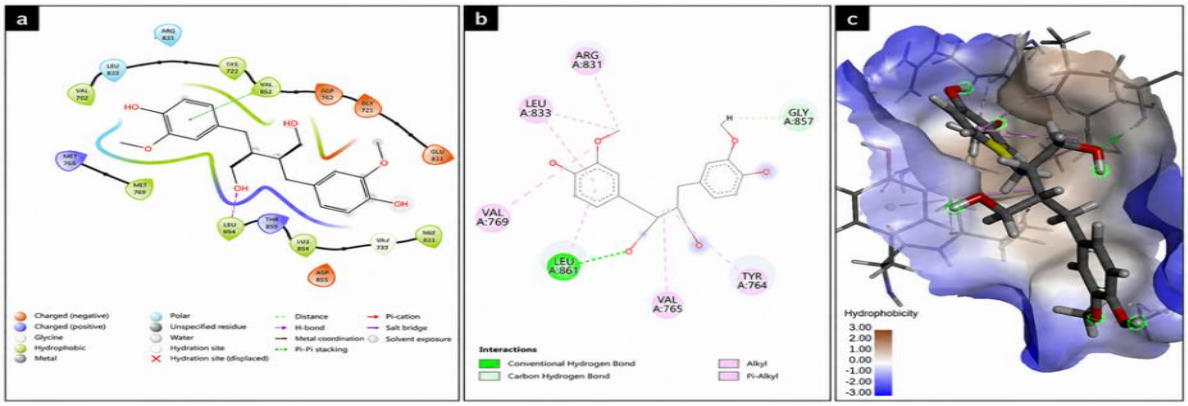

Figure 4: Molecular interaction analysis of Leuprolide (Reference) with the target protein. (a) Ligand-protein interaction diagram showing the types of interactions with surrounding amino acid residues. (b) 2D interaction diagram illustrating hydrogen bonds and hydrophobic contacts. (c) 3D hydrophobic surface representation of the binding pocket with the ligand (hydrophobicity scale: brown = hydrophobic; blue = hydrophilic).

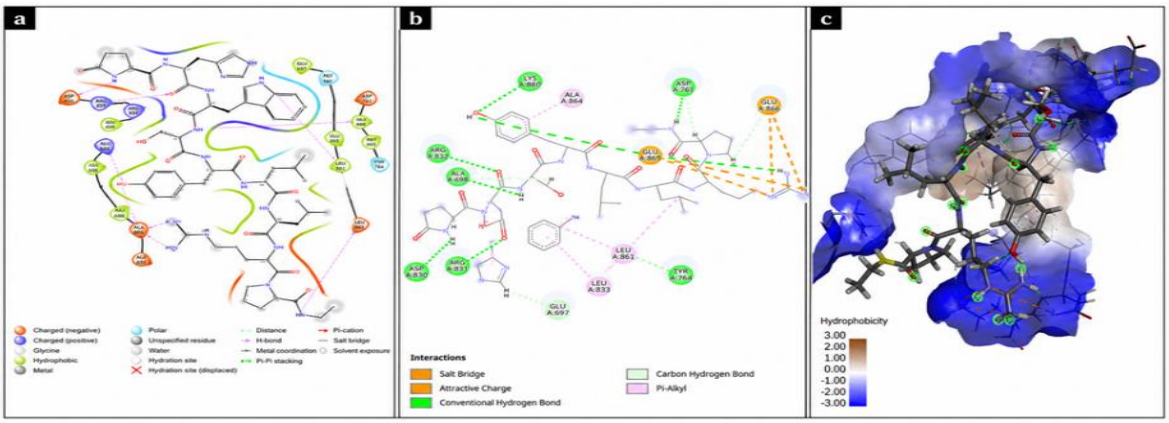

Figure 5: Molecular interaction analysis of 2,3-Bis[(4-hydroxy-3-methoxyphenyl)methyl]butane-1,4-diol, tetramethyl ether with the target protein. (a) Ligand-protein interaction diagram showing the types of interactions with surrounding amino acid residues. (b) 2D interaction diagram illustrating hydrogen bonds and hydrophobic contacts. (c) 3D hydrophobic surface representation of the binding pocket with the ligand (hydrophobicity scale: brown = hydrophobic; blue = hydrophilic).

Molecular Dynamics Simulation Analysis of 2,3-Bis[(4-hydroxy-3-methoxyphenyl)methyl]butane-1,4-diol, tetramethyl ether

A 100 ns molecular dynamics (MD) simulation was performed to evaluate the dynamic stability and interaction behaviour of the complex formed between 2,3-Bis[(4-hydroxy-3-methoxyphenyl)methyl]butane-1,4-diol, tetramethyl ether and the target protein (Fig. 6). The protein and ligand RMSD profiles (Fig. 6a) showed considerable fluctuations throughout the simulation, with the protein Cα RMSD generally occupying approximately 2-30 Å, although transient excursions approaching 45-47 Å were observed. The ligand RMSD displayed even greater variability, with values ranging from near 0 to approximately 90-95 Å. Thus, although the complex maintained recurring bound conformations during portions of the trajectory, the pronounced RMSD fluctuations indicate substantial conformational rearrangements rather than a uniformly equilibrated complex.

The residue-level RMSF profile (Fig. 6b) further demonstrated heterogeneous flexibility across the protein. Moderate fluctuations were observed over much of the sequence, whereas higher mobility occurred around residues 100-130, 150-170, and particularly toward the C-terminal region (>270), where RMSF values approached 40 Å. These regions therefore represent comparatively flexible segments of the protein during the simulation. Despite these fluctuations, the protein-ligand contact analysis (Fig. 6c) demonstrated recurrent interactions involving several residues. Notable interaction contributions were observed for LEU703/704, ASP761, TYR764, VAL765, SER768, ARG831, and related pocket residues. The contact timeline showed that interactions were maintained intermittently throughout the 100 ns trajectory, while the interaction-fraction histogram indicated that ASP761, TYR764, LEU704, ASN701/GLN701, and ARG831 contributed prominently to ligand recognition. These persistent or recurrent contacts suggest that the ligand repeatedly engaged important residues within the binding region despite the conformational fluctuations observed in the RMSD and RMSF analyses.

Analysis of protein secondary-structure elements (P-SSE; Fig. 6d) indicated that the protein retained substantial secondary-structural organization throughout the simulation, with alternating regions of α-helical and β-sheet/other secondary-structure components distributed across the sequence. In general, the MD trajectory demonstrates dynamic but persistent protein-ligand association, characterized by recurrent contacts within the binding region and retention of substantial secondary-structural elements.

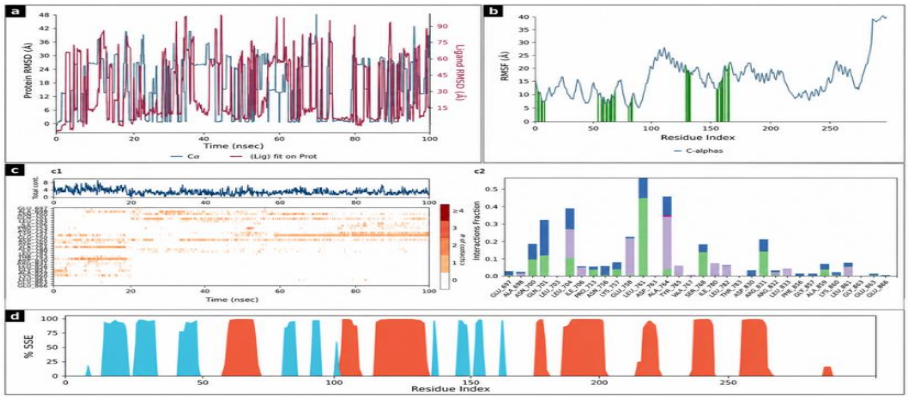

Figure 6: Molecular dynamics simulation analysis of the 2,3-bis[(4-hydroxy-3-methoxyphenyl)methyl]butane-1,4-diol, tetramethyl ether-target protein complex over 100 ns. (a) Protein and ligand RMSD profiles; (b) residue-wise Cα RMSF profile; (c) protein-ligand interaction analysis, comprising c1, contact timeline and c2, interaction-fraction histogram; and (d) protein secondary-structure element (P-SSE) profile throughout the simulation.

PASS-Based Interpretation of Fibroid-Relevant Activities
A comparative PASS activity profile of leuprolide (reference drug) and 2,3-bis[(4-hydroxy-3-methoxyphenyl)methyl]butane-1,4-diol, tetramethyl ether, expressed as predicted activity (Pa) and inactivity (Pi) probabilities (Table 4). Leuprolide showed strong predictions for immunostimulant (Pa/Pi = 0.802/0.009), GnRH agonist (0.720/0.000), releasing hormone agonist (0.612/0.003), and fibroblast growth factor agonist (0.601/0.017) activities. In comparison, the test compound exhibited predicted activities for ovulation inhibition (0.482/0.068), gonadotropin antagonism (0.445/0.035), menopausal disorders treatment (0.428/0.038), apoptosis agonism (0.436/0.057), and antineoplastic activity (0.264/0.123). Notably, the test compound showed a gonadotropin-antagonist prediction (Pa = 0.445; Pi = 0.035), which may be relevant to the endocrine regulation associated with hormone-responsive uterine fibroids. The predicted apoptosis agonist and antineoplastic activities may additionally be relevant to the abnormal cellular proliferation and impaired apoptotic processes characteristic of fibroid tissue. However, the PASS predictions represent in silico probabilities and should not be interpreted as direct evidence of anti-fibroid efficacy.

Table 4: PASS Activities Relevant to Uterine Fibroids

Activity	Leuprolide Pa/Pi	2,3-Bis[(4-hydroxy-3-methoxyphenyl)methyl]butane-1,4-diol, tetramethyl ether Pa/Pi
Apoptosis agonist	-	0.436/0.057
Antineoplastic	-	0.264/0,123
Immunostimulant	0.802/0.009	-
Luteinizing hormone-releasing hormone (GnRH) agonist	0.720/0.000	0.160/0.016
Releasing hormone agonist	0.612/0.003	-
Fibroblast growth factor agonist	0.601/0.017	-
Ovulation inhibitor	-	0.482/0.068
Gonadotropin antagonist	0.400/0.058	0.445/0.035
Menopausal disorders treatment	-	0.428/0.038
Follicle-stimulating hormone agonist	0.385/0.004	-

Acute Toxicity Prediction
The predicted acute toxicity profiles of leuprolide and the prioritized *Acanthus montanus* phytochemical, 2,3-bis[(4-hydroxy-3-methoxyphenyl)methyl]butane-1,4-diol, tetramethyl ether, are presented in Table 5. The predicted oral LD_{50} was 2,400 mg/kg for leuprolide and 2,000 mg/kg for the phytochemical, corresponding to toxicity classes 5 and 4, respectively. Both compounds were predicted to be non-toxic following acute inhalation and oral exposure, while the acute dermal toxicity predictions were also non-toxic.
For irritation and sensitization endpoints, leuprolide was predicted to be toxic for eye irritation/corrosion, whereas the phytochemical was predicted to be non-toxic for this endpoint. Conversely, the phytochemical was predicted to be a skin sensitizer, while leuprolide was classified as a non-sensitizer. Both compounds produced negative predictions for skin irritation and corrosion. Invariably, the prioritized phytochemical showed a comparatively lower predicted LD_{50} and higher toxicity class than leuprolide, indicating a need for careful toxicological evaluation despite its favourable predictions for acute oral, inhalation, dermal toxicity and eye irritation. These computational findings provide preliminary safety information but require experimental validation before any definitive toxicological conclusions can be drawn.

Table 5: ProTox-3.0 and StopTox predicted acute toxicity parameters for Leuprolid (Reference), Benzaldehyde, 4,5-dihydroxy-2,3-dimethoxy- and 2-(4-Bromophenyl)-5-hydroxypyrimidine

	Leuprolide	2,3-Bis[(4-hydroxy-3-methoxyphenyl)methyl]butane-1,4-diol, tetramethyl ether
Predicted LD_{50} (mg/kg)	2,400	2,000
Predicted Toxicity Class	5	4
Acute Inhalation Toxicity	Non-toxic	Non-toxic
Acute Oral Toxicity	Non-toxic	Non-toxic
Acute Dermal Toxicity	Non-toxic	Non-toxic
Eye Irritation and Corrosion	Toxic	Non-toxic
Skin Sensitization	Non-sensitizer	Sensitizer
Skin Irritation and Corrosion	Negative	Negative

Discussion
The present study employed an integrated computational workflow combining GC-MS profiling, ADME and drug-likeness assessment, network pharmacology, molecular docking, molecular dynamics (MD) simulation, PASS activity prediction, and toxicity profiling to investigate the potential of Acanthus montanus leaf phytochemicals against uterine fibroids. Ethanol extraction yielded 28.2% (w/w) crude extract, while GC-MS analysis identified 20 putative phytoconstituents comprising predominantly terpenoids, fatty acids, long-chain alcohols, aldehydes, esters, and oxygenated aromatic compounds. Notably, 2,3-bis[(4-hydroxy-3-methoxyphenyl)methyl]butane-1,4-diol, tetramethyl ether (hereafter, the tetramethyl ether derivative) showed a high library similarity of 95% and subsequently emerged as the most consistent docking candidate among the evaluated

phytochemicals. The collective findings provide computational evidence that constituents of A. montanus may influence several molecular processes implicated in uterine fibroid biology, although the results should be regarded as hypothesis-generating rather than proof of therapeutic efficacy.

The phytochemical composition provides a plausible biochemical basis for the observed computational activities. The extract contained neophytadiene, n-hexadecanoic acid, tridecanoic acid, long-chain alcohols, unsaturated fatty-acid derivatives, diterpenoid/terpenoid constituents, and the tetramethyl ether derivative. Several of these chemical classes have been associated with antioxidant, anti-inflammatory, antiproliferative, and hormone-modulating properties, which are mechanistically relevant to leiomyoma development. In particular, oxidative stress and chronic inflammatory signaling can promote cellular proliferation, extracellular-matrix accumulation, and activation of profibrotic pathways, including TGF-β-associated signaling . he occurrence of chemically diverse constituents in A. montanus therefore supports the possibility of a multi-component pharmacological effect rather than dependence on a single molecular target. This interpretation is consistent with the recognized complexity of uterine fibroid pathogenesis, which involves interactions among steroid hormones, growth factors, inflammation, extracellular-matrix remodeling, and altered cellular proliferation (Dolmans et al., 2024; Moravek & Bulun, 2015).

The ADME analysis further supported the prioritization of several constituents. Fourteen of the 20 identified compounds (70%) exhibited high predicted gastrointestinal absorption, whereas six compounds showed low predicted absorption and failed the applied drug-likeness criteria. Importantly, the tetramethyl ether derivative exhibited high predicted gastrointestinal absorption, no violations of the evaluated drug-likeness rules, and no predicted PAINS alerts. The absence of PAINS alerts is particularly relevant because nonspecific assay-interfering structures may generate misleading biological signals during early drug discovery (Capuzzi et al., 2017; Yang et al., 2021). Similarly, favourable predicted pharmacokinetic characteristics and compliance with commonly applied drug-likeness filters provide useful preliminary criteria for prioritizing natural-product candidates for experimental investigation (Daina et al., 2017; Idakwoji et al., 2026; Kim et al., 2025). Nevertheless, predicted gastrointestinal absorption should not be equated with demonstrated systemic bioavailability because absorption, metabolism, plasma protein binding, tissue distribution, and metabolic stability cannot be established from in silico descriptors alone.

Network pharmacology provided further evidence for the potential involvement of *A. montanus* constituents in fibroid-associated molecular processes. Of the 970 predicted phytochemical-associated targets and 227 uterine fibroid-associated genes, 25 targets overlapped, representing 2.6 and 11.0% of the respective datasets. The STRING network demonstrated substantial interconnectivity among these targets, with prominent involvement of PI3K-related proteins, cell-cycle regulators, hormone-associated proteins, DNA-repair proteins, and growth-signaling molecules. The PIK3CA/PIK3CB/PIK3CD and PIK3R1/PIK3R2/PIK3R3 clusters were particularly prominent, while ESR2, PGR, CDK4, PARP1, TERT, RET, CASR, KIT, and GNRHR were connected to several other network components. These observations are biologically relevant because estrogen and progesterone signaling constitute major determinants of leiomyoma growth, while PI3K/AKT, EGFR, MAPK, and cell-cycle pathways contribute to proliferation and survival of fibroid cells (Gekle et al., 2023; Saini et al., 2026; Wang et al., 2026). Thus, the network topology supports a polypharmacological interpretation in which several phytochemicals may simultaneously influence interconnected processes rather than acting through an isolated target. Such a mechanism is consistent with the network-pharmacology paradigm proposed for complex diseases in which modulation of multiple functionally related targets may be advantageous over highly selective single-target intervention (Hopkins, 2008; Hussein et al., 2026; Wang et al., 2025).

The pathway-enrichment analysis strengthened this interpretation by identifying multiple signaling pathways associated with the 25 shared targets. Particularly notable were PI3K-Akt, MAPK, Ras, Rap1, calcium, estrogen, hormone, microRNA, and EGFR-related signaling pathways, together with cancer-associated pathways and central carbon metabolism. Central carbon metabolism in cancer and non-small-cell lung cancer pathways showed approximately 65-fold enrichment, while melanoma, breast cancer, endocrine resistance, and glioma pathways also showed substantial enrichment. Although uterine fibroids are benign tumors, they exhibit several molecular characteristics associated with neoplastic biology, including dysregulated cellular proliferation, altered growth-factor signaling, angiogenesis, and extracellular-matrix remodeling (Mukherjee, 2025; Munro et al., 2025). The enrichment of PI3K/AKT and MAPK signaling is particularly noteworthy because these pathways participate in cellular growth, survival, and fibrotic responses, while TGF-β signaling has an established role in extracellular-matrix deposition and leiomyoma biology (Hu et al., 2025; Pandey et al., 2026). The convergence of these pathways suggests that the biological effects of *A. montanus* may involve coordinated modulation of hormone-responsive, proliferative, metabolic, and fibrotic processes.

Molecular docking provided an additional level of target-specific evidence. Leuprolide, used as the reference compound, demonstrated the strongest docking scores, with Glide SP and XP scores of -8.290 and -8.145 kcal/mol, respectively, and corresponding MM-GBSA binding energies of -40.63 and -55.42 kcal/mol. Among the *A. montanus* constituents, the tetramethyl ether derivative produced the most consistent docking scores, with SP and XP scores of -4.772 and -4.511 kcal/mol, respectively. Although its docking scores were weaker than those of leuprolide, the compound showed a comparatively favourable and consistent binding profile relative to the other prioritized phytochemicals. Interestingly, supraene produced more favourable MM-GBSA values (-44.64 and -47.39 kcal/mol for SP and XP, respectively), demonstrating that docking score and MM-GBSA estimates may rank compounds differently. This observation emphasizes the importance of considering multiple complementary computational descriptors rather than relying on a single scoring function.

The binding-mode analysis further demonstrated that the tetramethyl ether derivative was accommodated within the target binding pocket through a combination of conventional hydrogen bonds, carbon-hydrogen interactions, π-alkyl contacts, attractive-charge/salt-bridge interactions, and hydrophobic contacts. Interactions involving LYS860, ASP761, GLU865, GLU866, TYR764, LEU861, LEU833, ALA864, ARG831/832, and ASP830 were observed, indicating that both polar and hydrophobic forces contributed to ligand recognition. Such interaction diversity may be advantageous for maintaining ligand recognition within a chemically heterogeneous binding cavity. Similar computational observations have been reported for

phytochemicals investigated against fibroid-associated molecular targets, including epigallocatechin gallate (EGCG), while clinical evidence has also indicated that green tea extract may reduce fibroid volume (de Mezer et al., 2025; Islam et al., 2023). Curcumin has likewise demonstrated antifibrotic and antiproliferative effects through modulation of NF-κB and TGF-β-associated mechanisms (Olivera et al., 2012; Yang et al., 2026). These precedents provide biological context for the present docking observations, although structural similarity or comparable computational binding should not be interpreted as evidence that the tetramethyl ether derivative possesses equivalent clinical activity.

The 100-ns molecular dynamics simulation provided important information beyond the static docking analysis. In contrast to a uniformly stable complex, the RMSD trajectories demonstrated substantial conformational fluctuations in both the protein and ligand during the simulation. Protein Cα RMSD generally ranged between approximately 2 and 30 Å, with transient excursions approaching 45-47 Å, whereas ligand RMSD exhibited considerably larger fluctuations, reaching approximately 90-95 Å at some points. Therefore, the MD trajectory should not be interpreted as evidence of uniformly rigid structural stability. Rather, the results indicate substantial conformational rearrangement and dynamic sampling of alternative ligand-bound states. This distinction is important because MD simulation provides a dynamic representation of molecular behaviour that cannot be captured by a single docking pose (Nivatya et al., 2025; Singh et al., 2022).

Despite the pronounced RMSD fluctuations, the residue-level RMSF analysis indicated that protein flexibility was heterogeneous rather than uniformly increased. Elevated mobility was particularly evident around residues 100-130, 150-170, and toward the C-terminal region beyond residue 270, whereas other regions displayed comparatively lower fluctuations. Importantly, the high flexibility did not eliminate protein–ligand recognition. Recurrent contacts involving LEU703/704, ASP761, TYR764, VAL765, SER768, ARG831, and other binding-site residues were observed throughout the trajectory. ASP761, TYR764, LEU704, ASN701/GLN701, and ARG831 made particularly prominent contributions to the interaction profile. Thus, the MD results suggest a dynamic but persistent association, in which the ligand undergoes substantial positional and conformational changes while repeatedly re-engaging, important residues within the binding region.

The protein secondary-structure analysis provides additional context for interpreting the apparently large RMSD values. Despite the substantial backbone fluctuations, the protein retained considerable secondary-structural organization, with α-helical and β-sheet/other secondary-structure elements persisting throughout the simulation. Collectively, the RMSD, RMSF, contact timeline, interaction-fraction histogram, and P-SSE profiles therefore suggest that the complex remained dynamically associated rather than completely dissociating. Nevertheless, because the RMSD excursions were relatively large, additional replicate simulations and longer trajectories would be valuable before describing the complex as conformationally stable in the strict thermodynamic sense.

PASS prediction provided complementary functional evidence. The reference drug leuprolide showed the expected endocrine-related activity profile, including GnRH agonism (Pa/Pi = 0.720/0.000), releasing-hormone agonism (0.612/0.003), fibroblast growth-factor agonism (0.601/0.017), and follicle-stimulating-hormone agonism (0.385/0.004). In contrast, the tetramethyl ether derivative showed predicted ovulation-inhibitory activity (0.482/0.068), gonadotropin-antagonist activity (0.445/0.035), menopausal-disorder-treatment activity (0.428/0.038), apoptosis-agonist activity (0.436/0.057), and antineoplastic activity (0.264/0.123). Among these predictions, gonadotropin antagonism is particularly relevant to hormone-responsive fibroid biology, while the apoptosis and antineoplastic predictions are mechanistically relevant to the excessive proliferation and altered cell-death balance characteristic of leiomyoma. The biological relevance of apoptosis is supported by evidence that fibroid tissues exhibit altered apoptotic regulation compared with normal myometrium (Horak et al., 2012; Lee et al., 2020). However, the lower Pa values for apoptosis and antineoplastic activity indicate that these predictions are substantially weaker than the classical endocrine predictions obtained for leuprolide. PASS outputs should therefore be interpreted as probability-based activity hypotheses and not as direct evidence of anti-fibroid efficacy.

The PASS results also emphasize a potentially important mechanistic distinction between the reference drug and the plant-derived candidate. Leuprolide predominantly displayed endocrine activity consistent with its established GnRH-mediated pharmacology, whereas the tetramethyl ether derivative exhibited a broader but weaker spectrum encompassing endocrine modulation, apoptosis, and antineoplastic activity. This may support the hypothesis that *A. montanus* constituents could influence fibroid biology through mechanisms extending beyond direct hormonal suppression. Such a multi-target strategy is conceptually attractive because uterine fibroids are regulated by interconnected hormonal, proliferative, inflammatory, metabolic, and extracellular-matrix pathways (Hussein et al., 2026; Wang et al., 2025). However, whether these predicted activities occur at biologically relevant concentrations remains to be determined experimentally.

The toxicity assessment provides a preliminary indication of the safety profile of the prioritized compound. The predicted oral LD_{50} of the tetramethyl ether derivative was 2,000 mg/kg, corresponding to toxicity class 4, compared with 2,400 mg/kg and toxicity class 5 for leuprolide. Both compounds were predicted to be non-toxic following acute oral, inhalation, and dermal exposure. The tetramethyl ether derivative was also predicted to be non-toxic for eye irritation/corrosion and negative for skin irritation/corrosion. However, it was predicted to be a skin sensitizer, highlighting a potential dermal safety concern. These findings indicate a generally acceptable preliminary acute-toxicity profile but do not establish overall safety. Computational toxicity models are valuable for early-stage prioritization, but their predictions require confirmation using appropriate in vitro and in vivo toxicological assays (Ajisafe et al., 2025; Banerjee et al., 2018; Sheng et al., 2025).

The integrated findings are also consistent with the broader literature on phytotherapeutic approaches to uterine fibroids. Green tea catechins, vitamin D, curcumin, and other botanical compounds have been investigated for their ability to modulate oxidative stress, inflammation, steroid-hormone signaling, apoptosis, and extracellular-matrix remodeling (Ahmed, 2025; Alam et al., 2024). In particular, EGCG has demonstrated encouraging effects on fibroid biology and fibroid volume in clinical investigation, whereas curcumin has shown antifibrotic and antiproliferative activity in experimental models (Islam et al., 2023; Olivera et al., 2012; Yang et al., 2026). The present results extend this concept by identifying a chemically characterized *A. montanus* extract containing multiple constituents with predicted interactions across interconnected fibroid-related targets. The potential

advantage of such a phytochemical mixture may therefore arise from complementary or synergistic modulation of several disease-associated pathways rather than from a single highly potent constituent.

Notwithstanding these encouraging findings, several limitations should be considered. First, the study is entirely computational and therefore cannot establish biological efficacy, cellular selectivity, or clinical benefit. Second, GC-MS library identification represents putative chemical identification and should ideally be confirmed using authentic standards and complementary spectroscopic approaches. Third, network pharmacology and target-prediction methods are dependent on database coverage and algorithmic assumptions, while molecular docking provides relative estimates of binding rather than experimentally determined affinities. Fourth, the substantial RMSD fluctuations observed during the 100-ns MD trajectory indicate that additional replicate simulations, longer trajectories, and potentially free-energy calculations would strengthen the assessment of binding persistence. Fifth, predicted ADME and toxicity properties require experimental confirmation because metabolism, tissue distribution, bioavailability, and long-term toxicity cannot be reliably inferred solely from computational models. Finally, the biological relevance of the PASS predictions requires validation using uterine leiomyoma cell models, normal myometrial cells, appropriate animal models, and ultimately well-designed clinical studies. Henceforth, the integrated computational evidence supports *A. montanus* as a promising source of phytochemicals with potential relevance to uterine fibroid biology. The study identified 25 shared fibroid-associated targets, including interconnected hormone-, PI3K/AKT-, EGFR-, cell-cycle-, and DNA-repair-related proteins, while pathway analysis implicated estrogen, PI3K-Akt, MAPK, Ras, calcium, hormone, and cancer-associated signaling. The tetramethyl ether derivative was particularly noteworthy because of its high-confidence GC–MS identification, favourable predicted gastrointestinal absorption, absence of drug-likeness violations and PAINS alerts, comparatively strong docking performance among the tested phytochemicals, recurrent protein–ligand interactions during MD simulation, and relevant PASS predictions for gonadotropin antagonism, apoptosis, and antineoplastic activity. Nevertheless, the MD trajectory indicates a dynamic rather than rigidly stable complex, and the relatively modest PASS probabilities for apoptosis and antineoplastic activities warrant cautious interpretation. Taken together, the findings support the hypothesis that *A. montanus* may exert anti-fibroid effects through coordinated modulation of endocrine signaling, cellular proliferation, apoptosis, and fibrotic pathways, but experimental validation is essential before these computational observations can be translated into therapeutic claims.

CONCLUSION

This study provides integrated computational evidence that *Acanthus montanus* is a promising source of phytochemicals with potential relevance to uterine fibroid biology. GC-MS profiling identified a chemically diverse group of constituents, while ADME and drug-likeness analyses indicated favourable pharmacokinetic characteristics for several compounds, particularly 2,3-bis[(4-hydroxy-3-methoxyphenyl)methyl]butane-1,4-diol, tetramethyl ether. Network pharmacology identified 25 shared targets linking the phytochemical constituents with uterine fibroid-associated genes, with enrichment of hormone-related, PI3K-Akt, MAPK, EGFR, cell-cycle, and other pathways implicated in leiomyoma development.

Molecular docking further prioritized the tetramethyl ether derivative based on its comparatively favourable binding profile and interactions with several residues within the target binding site. The 100-ns molecular dynamics simulation indicated persistent protein–ligand contacts and retention of secondary structural elements, although substantial RMSD fluctuations demonstrated that the complex was dynamically flexible rather than uniformly rigid. PASS prediction additionally suggested potential endocrine-modulating, apoptosis-related, and antineoplastic activities, providing mechanistic hypotheses relevant to fibroid biology. The compound also showed a relatively favourable predicted acute toxicity profile, although its predicted skin-sensitizing potential warrants further investigation.

In general, the findings suggest that the potential anti-fibroid activity of *A. montanus* may involve multitarget modulation of hormonal signaling, cellular proliferation, apoptosis, and fibrotic processes, rather than interaction with a single molecular pathway. However, these conclusions remain predictive and cannot establish therapeutic efficacy or safety. Experimental validation using uterine leiomyoma cell models, animal studies, and subsequent pharmacological and toxicological investigations is therefore essential to confirm the identified mechanisms and determine the therapeutic relevance of the prioritized phytochemicals.

REFERENCES

Ahmed, M. (2025). Targeting aging pathways with natural compounds: a review of curcumin, epigallocatechin gallate, thymoquinone, and resveratrol. *Immunity & Ageing*, *22*(1), 28. https://doi.org/10.1186/s12979-025-00522-y

Ajisafe, O. M., Adekunle, Y. A., Egbon, E., Ogbonna, C. E., & Olawade, D. B. (2025). The role of machine learning in predictive toxicology: A review of current trends and future perspectives. *Life Sciences*, *378*, 123821. https://doi.org/https://doi.org/10.1016/j.lfs.2025.123821

Alam, M., Gulzar, M., Akhtar, M. S., Rashid, S., Zulfareen, Tanuja, Shamsi, A., & Hassan, M. I. (2024). Epigallocatechin-3-gallate therapeutic potential in human diseases: molecular mechanisms and clinical studies. *Molecular Biomedicine*, *5*(1), 73. https://doi.org/10.1186/s43556-024-00240-9

Aljawobaei, W., Ali, S. S. M., Thippeswamy, N. B., & Achur, R. (2025). Molecular docking and ADMET analysis of bioactive compounds from Simarouba glauca leaf extracts for anti-inflammatory and antioxidant activities. *Discover Applied Sciences*, *7*(10), 1082. https://doi.org/10.1007/s42452-025-07429-9

Asiamah, I., Obiri, S. A., Tamekloe, W., Armah, F. A., & Borquaye, L. S. (2023). Applications of molecular docking in natural products-based drug discovery. *Scientific African*, *20*, e01593. https://doi.org/https://doi.org/10.1016/j.sciaf.2023.e01593

Banerjee, P., Eckert, A., Schrey, A., & Preissner, R. (2018). ProTox-II: A webserver for the prediction of toxicity of chemicals. *Nucleic Acids Research*, *46*. https://doi.org/10.1093/nar/gky318

Capuzzi, S. J., Muratov, E. N., & Tropsha, A. (2017). Phantom PAINS: Problems with the Utility of Alerts for Pan-

Assay INterference CompoundS. *J Chem Inf Model*, *57*(3), 417-427. https://doi.org/10.1021/acs.jcim.6b00465

Daina, A., Michielin, O., & Zoete, V. (2017). SwissADME: a free web tool to evaluate pharmacokinetics, drug-likeness and medicinal chemistry friendliness of small molecules. *Scientific Reports*, *7*(1), 42717. https://doi.org/10.1038/srep42717

de Mezer, M., Markowska, A., Pietras, J., Naskręt-Grochowalska, A., Gryboś, M., Markowska, J., & Sajdak, S. (2025). The role of epigallocatechin gallate (EGCG) in uterine myomas. *Biomedicine & Pharmacotherapy*, *189*, 118345. https://doi.org/https://doi.org/10.1016/j.biopha.2025.118345

Dolmans, M.-M., Petraglia, F., Catherino, W. H., & Donnez, J. (2024). Pathogenesis of uterine fibroids: current understanding and future directions. *Fertility and Sterility*, *122*(1), 6-11. https://doi.org/https://doi.org/10.1016/j.fertnstert.2024.02.048

Farhadi, B., Beygisangchin, M., Ghamari, N., Jakmunee, J., & Tang, T. (2025). Molecular dynamics simulations of proteins: an in-depth review of computational strategies, structural insights, and their role in medicinal chemistry and drug development. *Biological Cybernetics*, *119*(4), 28. https://doi.org/10.1007/s00422-025-01026-0

Gekle, M., Dubourg, V., Schwerdt, G., Benndorf, R. A., & Schreier, B. (2023). The role of EGFR in vascular AT1R signaling: From cellular mechanisms to systemic relevance. *Biochemical Pharmacology*, *217*, 115837. https://doi.org/https://doi.org/10.1016/j.bcp.2023.115837

Grewal, S., Deswal, G., Grewal, A. S., & Guarve, K. (2025). Chapter Eight - Molecular dynamics simulations: Insights into protein and protein ligand interactions. In C. V. Narayan, S. Verma, A. S. Grewal, N. Singh, & H. Nimesh (Eds.), *Advances in Pharmacology* (Vol. 103, pp. 139-162). Academic Press. https://doi.org/https://doi.org/10.1016/bs.apha.2025.01.007

Hopkins, A. L. (2008). Network pharmacology: the next paradigm in drug discovery. *Nature Chemical Biology*, *4*(11), 682-690. https://doi.org/10.1038/nchembio.118

Horak, P., Mara, M., Dundr, P., Kubinova, K., Kuzel, D., Hudecek, R., & Chmel, R. (2012). Effect of a selective progesterone receptor modulator on induction of apoptosis in uterine fibroids in vivo. *Int J Endocrinol*, *2012*, 436174. https://doi.org/10.1155/2012/436174

Hu, H., Chen, Y., Hong, B., Liu, J., Jiang, Y., Yu, Z., Xiao, Z.-J., & Li, J. (2025). A four-gene signature identified by integrated transcriptomic analysis for differential diagnosis and prognosis of uterine smooth muscle tumors [Original Research]. *Frontiers in Oncology*, *Volume 15 - 2025*. https://www.frontiersin.org/journals/oncology/articles/10.3389/fonc.2025.1591875

Hussein, F., Elamin, O., Al-Hendy, A., & Mousa, M. (2026). Multi-omics Approaches for Biomarker Discovery of Uterine Fibroids: A Systematic Review. *Advances in Therapy*, *43*(6), 2474-2495. https://doi.org/10.1007/s12325-026-03569-5

Idakwoji, P. A., Tukur, U., Onwukwe, B. O., Agboola, J. B., Onugwu, E. O., Iyiola, A. T., Amadi, B. E., Onoja, A. O., Ali, A. S., Ojo, S. S., Adeyeye, M. A., & Muhammed, H. (2026). Phytochemicals as promising lead compounds for drug discovery: A comprehensive review of mechanisms and pharmacological potentials. *Letters in Drug Design & Discovery*, *23*(1), 100363. https://doi.org/https://doi.org/10.1016/j.lddd.2026.100363

Idu, M., Ojoba, P., & Gabriel, B. O. (2022). Acanthus montanus (Nees) T. Anderson: Review. *6*, 21-34.

Islam, M. S., Parish, M., Brennan, J. T., Winer, B. L., & Segars, J. H. (2023). Targeting fibrotic signaling pathways by EGCG as a therapeutic strategy for uterine fibroids. *Sci Rep*, *13*(1), 8492. https://doi.org/10.1038/s41598-023-35212-6

Kim, H. K., Kim, S. J., Gil, W. J., & Yang, C.-S. (2025). Exploring the therapeutic potential of phytochemicals: challenges and strategies for clinical translation. *Phytomedicine*, *145*, 157090. https://doi.org/https://doi.org/10.1016/j.phymed.2025.157090

Lee, J. W., Choi, H. J., Kim, E. J., Hwang, W. Y., Jung, M. H., & Kim, K. S. (2020). Fisetin induces apoptosis in uterine leiomyomas through multiple pathways. *Sci Rep*, *10*(1), 7993. https://doi.org/10.1038/s41598-020-64871-y

Moravek, M. B., & Bulun, S. E. (2015). Endocrinology of uterine fibroids: steroid hormones, stem cells, and genetic contribution. *Curr Opin Obstet Gynecol*, *27*(4), 276-283. https://doi.org/10.1097/gco.0000000000000185

Mukherjee, P. (2025). Genetic and biomarker approaches to uterine fibroids: toward precision medicine [Mini Review]. *Frontiers in Global Women's Health*, *Volume 6 - 2025*. https://www.frontiersin.org/journals/global-womens-health/articles/10.3389/fgwh.2025.1581823

Munro, M. G., Tchaikovski, S. N., & Murji, A. (2025). The epidemiology and pathogenesis of uterine fibroids. *International Journal of Gynecology & Obstetrics*, *171*(3), 1029-1045. https://doi.org/https://doi.org/10.1002/ijgo.70527

Nivatya, H. K., Singh, A., Kumar, N., Sonam, Sharma, L., Singh, V., Mishra, R., Gaur, N., & Mishra, A. K. (2025). Assessing molecular docking tools: understanding drug discovery and design. *Future Journal of Pharmaceutical Sciences*, *11*(1), 111. https://doi.org/10.1186/s43094-025-00862-y

Okoli, C. O., Akah, P. A., Onuoha, N. J., Okoye, T. C., Nwoye, A. C., & Nworu, C. S. (2008). Acanthus montanus: An experimental evaluation of the antimicrobial, anti-inflammatory and immunological properties of a traditional remedy for furuncles. *BMC Complementary and Alternative Medicine*, *8*(1), 27. https://doi.org/10.1186/1472-6882-8-27

Olivera, A., Moore, T. W., Hu, F., Brown, A. P., Sun, A., Liotta, D. C., Snyder, J. P., Yoon, Y., Shim, H., Marcus, A. I., Miller, A. H., & Pace, T. W. (2012). Inhibition of the NF-κB signaling pathway by the curcumin analog, 3,5-Bis(2-pyridinylmethylidene)-4-piperidone (EF31): anti-inflammatory and anti-cancer properties. *Int Immunopharmacol*, *12*(2), 368-377. https://doi.org/10.1016/j.intimp.2011.12.009

Oshadu, D. O., Ajanusi, J. O., Chiezey, P. N., Abubakar, M. S., Tanko, J. T., Sambo, S. J., & Mohammed, B. (2022). Toxicological Evaluation and Therapeutic Index of Ethanolic Leaf Extract of Acanthus montanus (Acanthaceae) in Mice. *Journal of Pharmacology and Toxicology*, *17*(1), 28-35. https://doi.org/10.3923/jpt.2022.28.35

Pandey, V., Patel, Y., Tiwari, S., Rani, A., Rai, S., Agarwal, S., Tripathi, A., & Dubey, P. K. (2026). MED12 somatic mutation promotes human uterine leiomyoma's growth by trigging canonical Wnt4/β-catenin and TGF-β signaling through the EMT pathway. *Journal of Endometriosis and Uterine Disorders*, *13*, 100137. https://doi.org/https://doi.org/10.1016/j.jeud.2025.100137

Saini, K., Singh, S., & Garg, N. (2026). Progesterone and estrogen signaling in uterine fibroids: A tale of two interconnected pathways. *The Journal of Steroid Biochemistry and Molecular Biology*, *262*, 107036. https://doi.org/https://doi.org/10.1016/j.jsbmb.2026.107036

Sheng, Q.-S., Liu, B., Wang, X., Hua, L., Zhao, S.-C., Sun, X.-Z., Li, M.-Y., Zhang, X.-Y., Wang, J.-X., & Hu, P.-L. (2025). Revolutionizing toxicological risk assessment: integrative advances in new approach methodologies (NAMs) and precision toxicology. *Archives of Toxicology*, *99*(12), 4697-4707. https://doi.org/10.1007/s00204-025-04169-y

Singh, S., Bani Baker, Q., & Singh, D. B. (2022). Chapter 18 - Molecular docking and molecular dynamics simulation. In D. B. Singh & R. K. Pathak (Eds.), *Bioinformatics* (pp. 291-304). Academic Press. https://doi.org/https://doi.org/10.1016/B978-0-323-89775-4.00014-6

Wang, C.-Y., Philpott, M., P O'Brien, D., Ndungu, A., Malzahn, J., Maritati, M., Mehta, N., Gamble, V., Martinez-Burgo, B., Bonham, S., Fischer, R., Garbutt, K., Becker, C. M., Manek, S., Harris, A. L., Sacher, F., Obendorf, M., Schmidt, N., Müller, J., . . . Cribbs, A. P. (2025). A systems-based approach to uterine fibroids identifies differential splicing associated with abnormal uterine bleeding. *Communications Medicine*, *5*(1), 318. https://doi.org/10.1038/s43856-025-01051-x

Wang, L., Geng, M., Wei, L., Wang, S., Wang, W., & Liu, X. (2026). Multidimensional regulation of estrogen signaling in pelvic floor connective tissue homeostasis and remodeling [Review]. *Frontiers in Immunology*, *Volume 17 - 2026*. https://www.frontiersin.org/journals/immunology/articles/10.3389/fimmu.2026.1742246

Yang, Q.-m., Chen, Y., Xia, L.-h., Xu, H., Jin, X.-f., & Wu, Q. (2026). Curcumin Inhibits Fibroblast Differentiation and Epithelial-Mesenchymal Transition to Alleviate Adenomyosis through TGF-β1/Smad3 Pathway. *Chinese Journal of Integrative Medicine*, *32*(5), 407-414. https://doi.org/10.1007/s11655-025-4215-0

Yang, Z.-Y., Yang, Z.-J., He, J.-H., Lu, A.-P., Liu, S., Hou, T.-J., & Cao, D.-S. (2021). Benchmarking the mechanisms of frequent hitters: limitation of PAINS alerts. *Drug Discovery Today*, *26*(6), 1353-1358. https://doi.org/https://doi.org/10.1016/j.drudis.2021.02.003